CIRP Annals - Manufacturing Technology 70 (2021) 49–52

Contents lists available at ScienceDirect

CIRP Annals - Manufacturing Technology

journal homepage: https://www.editorialmanager.com/CIRP/default.aspx

Considering the influence of heating rate, complex hardening and dynamic strain aging in AISI 1045 machining: experiments and simulations

Friedrich Bleicher (2)[a,*], Christian Baumann[a], Stephan Krall[a], Steven P. Mates[b], Sibylle Herzig[c], Tim Alder[c], Norman Herzig[c]

[a] Institute of Production Engineering and Photonic Technologies, TU Wien, Austria
[b] National Institute of Standards and Technology, 100 Bureau Drive, Gaithersburg, MD, USA
[c] Nordmetall GmbH, Germany

ARTICLE INFO

Article history:
Available online 8 June 2021

Keywords:
Machining
Material
Modelling

ABSTRACT

In the modelling of machining operations, constitutive models must consider the material behavior subject to high plastic strains, high strain rates, high temperatures and high heating rates. A new material model for AISI 1045, which captures time-dependent plastic response associated with interrupted austenite transformation under short (sub-second) heating times, is deployed to simulate orthogonal cutting experiments. High speed video and digital image correlation measurements are used to capture chip behavior. The new model, which also includes complex strain hardening and dynamic strain aging effects, show better agreement with experiments at high cutting speeds compared with a basic Johnson-Cook material model from the literature.

1. Introduction and objective

Numerical simulations play a significant role in production engineering and particularly in the research on material processing technologies. In machining, materials are subjected to high plastic strains, high strain rates along with high temperatures and heating rates. To ensure good correlation of experimental and numerical results, appropriate material modelling is required. Constitutive models for numerical simulations of machining operations must be based on material data matching the loading conditions which are occurring in real cutting processes. Medium carbon steel, such as AISI 1045, exhibits complex plastic behavior for temperature and strain rate regimes important to machining due to phenomena such as dynamic strain aging (DSA) [1], also known as blue brittleness, and phase transformation. Many attempts to explore their influence on cutting mechanics through advanced material modelling have been documented [2–4]. However, predicting all aspects of the process (forces, temperatures and chip morphologies) remains elusive and motivates the present work.

2. Material model for AISI 1045 considering the heating rate

The effect of heating rate on the flow stress of AISI 1045 steel is shown in Fig. 1 which plots data obtained using a pulse-heated Kolsky bar technique [5]. The dynamic flow stress is increased above the transformation temperature (the A1 temperature, 712°C for this steel) for experiments with more rapid heating (via a temperature ramp lasting 1.0 s) compared to experiments where the temperature is held for 3.5 s before impact. This strengthening effect is attributable to incomplete

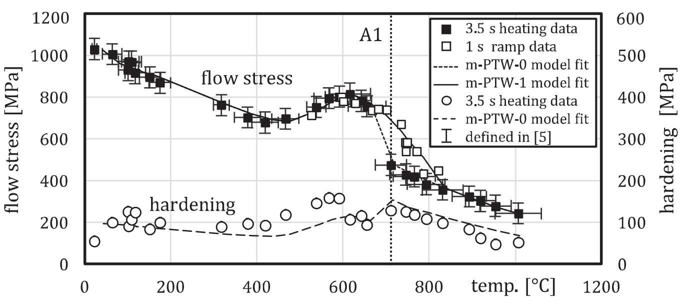

Fig. 1. Flow stress and model fits for 0.1 strain at 3 500 strain/s.

transformation of the microstructure from ferrite-pearlite to austenite. These ramp experiments are newly reported in this paper. In the plot of Fig. 1, "hardening" is defined as the increase in flow stress as the plastic strain increases from 0.075 to 0.2. Hardening is shown only for the 3.5 s heating data. Fig. 2 describes austenite transformation in AISI 1045 steel. Austenite rapidly consumes pearlite colonies in seconds, depending on heating rate, the interlamellar spacing and alloy content (Mn and Si) [6], after which the remaining ferrite is transformed more slowly (minutes to hours) as C and Mn diffuse into the ferrite [6]. Since the time available during machining is insufficient to fully or even partially transform steel despite temperatures often exceeding A1, it is of interest to explore how incomplete transformation in steel might influence metal cutting behavior. The ramp heating data of Fig. 1 provide a glimpse as to how incomplete transformation affects steel flow stress above A1, and these data are used here to calibrate a "transient" material model to compare cutting simulation results with the same model calibrated with the 3.5 s

* Corresponding author.
E-mail address: bleicher@ift.at (F. Bleicher).

https://doi.org/10.1016/j.cirp.2021.04.083
0007-8506/© 2021 Published by Elsevier Ltd on behalf of CIRP.

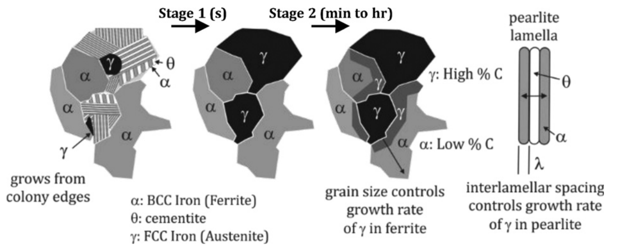

Fig. 2. Diffusion-controlled austenite transformation process in ferrite-pearlite carbon steel [6].

hold time data. Both models are compared to the results achieved by using the Johnson-Cook constitutive material model.

Aside from transformation behavior, the flow stress and hardening behavior of AISI 1045 over wide ranges of temperature and strain rate is quite complex, due in part to Dynamic Strain Aging (DSA) effects, and this behavior is beyond the capacity of general-purpose plasticity models to capture with a minimum set of fitting parameters. As such, a new constitutive model was developed, based on the Preston-Tonks-Wallace (PTW) model [7], which is designed to describe metal plasticity over a wide range of strain rates and temperatures. It uses Voce hardening to provide more flexible hardening evolution with temperature and strain rate compared to power law hardening models.

The PTW model defines a temperature (T) and strain-rate ($\dot{\gamma}$) dependent yield (τ_y) and saturation (τ_s) flow stress as follows:

$$\frac{\tau_y}{G(T)} = \left\{ y_0 - (y_0 - y_\infty) erf\left[k \frac{T_K}{T_{m,k}} \right] \right\} \cdot \left(1 + C \ln \frac{\dot{\gamma}}{\dot{\gamma}_0} \right)$$

$$\frac{\tau_s}{G(T)} = \left\{ s_0 - (s_0 - s_\infty) erf\left[k \frac{T_K}{T_{m,k}} \right] \right\} \cdot \left(1 + C \ln \frac{\dot{\gamma}}{\dot{\gamma}_0} \right)$$

Voce hardening is calculated by combining the yield and saturation stresses along with a hardening modulus, θ :

$$\frac{\tau}{G(T)} = \frac{\tau_y}{G(T)} + \int_0^\gamma \theta \frac{\tau_s - \tau}{\tau_s - \tau_y} \mathrm{d}\gamma$$

G(T) is the temperature-dependent shear modulus, T_K and $T_{m,K}$ are the temperature and melting temperature in K, respectively, and y_0, y_∞, s_0, s_∞, k, C, $\dot{\gamma}_0$ and θ are fitting parameters. τ and γ denote shear stress and shear strain, respectively, which convert to normal stress and normal strain via $\sigma = \sqrt{3}\tau$ and $\varepsilon = \gamma/\sqrt{3}$.

The strain-rate dependence in the new model is adapted from the work of Vural et al. [8] on low carbon steel. Finally, a Gaussian function is employed to capture strain-rate and temperature dependent DSA effects by modifying the yield, saturation and hardening behavior with a Gaussian function. An example of the modification of the yield stress is given below (parallel expressions are used for τ_s and θ).

$$\tau_{y-MOD} = \tau_y + \tau_{y,DSA}$$

$$\frac{\tau_{y,DSA}}{G(T)} = F(\dot{\gamma}) \frac{\tau_{y,0,DSA}}{G(T)} \exp\left[-\frac{(T - T_\mu(\dot{\gamma}))^2}{\delta^2} \right]$$

$$F(\dot{\gamma}) = 0.65 + 0.031 \ln\left(\frac{\dot{\gamma}}{\sqrt{3}} \right); \; T_\mu(\dot{\gamma}) = 414 + 25.668 \ln\left(\frac{\dot{\gamma}}{\sqrt{3}} \right)$$

Here, $\tau_{y,0,DSA}$ and δ are additional fitting parameters. The bottom two expressions represent the effect of strain rate on the mean temperature and magnitude of the DSA effects and are determined from literature data. Finally, austenite transformation is handled by fitting data above the A1 temperature separately. The resulting modified PTW model (m-PTW) uses 20 fitting parameters to capture AISI 1045 steel behavior up to 1000°C, strains up to 0.6 and strain rates up to 20 000 1/s. The parameters are listed in Table 1.

The highest strain rate data were obtained by using a combination of drop weight towers and Hopkinson bar setups. Transformation effects are explored by fitting separate models for the 3.5 s hold data (m-PTW-0) and the ramp data (m-PTW-1). Both fits are shown in Fig. 1. For the m-PTW-1 fit, A1 is increased to 800°C to reflect a delayed transformation of the microstructure under rapid heating. Further information on the model can be found in [9].

Table 1
Model coefficients for m-PTW-0 and m-PTW-1 models. A1 = 712°C for PTW-0 and 800°C for m-PTW-1. Temperatures are in°C.

	y_0	y_∞	s_0	s_∞	k	θ
(T < A1)	4.06e-3	0.0	7.26e-3	8.04e-7	0.748	0.0100
(T > A1)	5.74e-3	0.0	1.61e-3	1.83e-4	1.32	0.0168
	$\tau_{y,0,DSA}$/G(T)	$\tau_{s,0,DSA}$/G(T)	θ_{DSA}	δ [°C]		
m-PTW-0	3.15e-7	0.00342	0.0371	113.3		
m-PTW-1	3.05e-7	0.00298	0.0407	137.4		
G(T) [GPa]	$82.218 - 0.012085T - 5.7217 \cdot 10^{-5}T^2 + 2.6635 \cdot 10^{-8}T^3$					
	C	γ_0 [1/s]	T_m [°C]			
$\dot{\gamma} \leq 166$	$0.0177\dot{\gamma}^{0.0148}$	5.0e-6	1432			
$\dot{\gamma} > 166$	$0.0539\dot{\gamma}^{0.0555}$	1.65	1432			

3. Implementation in FEM-simulation

Plane strain (2D) and three-dimensional (3D) finite element analysis (FEA) was performed and compared to orthogonal cutting experiments in which cutting forces, temperatures and strain rates are measured, the latter using high-speed digital image correlation (DIC). Fig. 3 depicts the new model as implemented in the FEA simulations. For comparison, a basic Johnson-Cook model (JC, 5 fitting coefficients) developed for AISI 1045 (cf. [10]) is included to help assess any benefits of the more complex material model for the conditions studied. Fig. 3 compares the three models.

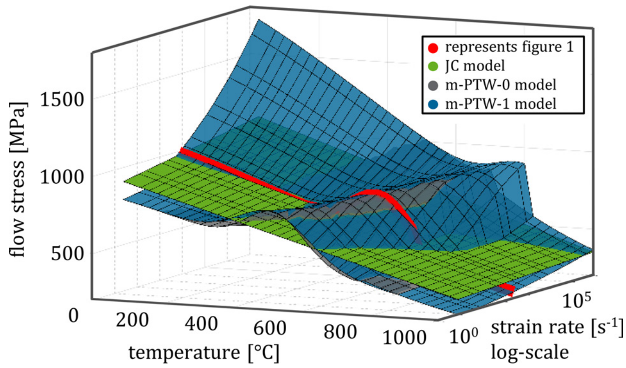

Fig. 3. Comparison of isothermal stress curves over temperature and strain rate at a strain of 0.1 for m-PTW and Johnson-Cook models.

The simulations were performed using DEFORM[1] v12.0.1 (from SFTC) for all three material models (JC, m-PTW-0, m-PTW-1). Temperature-dependent thermophysical properties, such as Young's modulus, heat capacity, density, thermal conductivity, etc., were calculated based on CalPhad method using JMatPro V11 and were transferred into DEFORM as a function of temperature.

Coulomb friction is modelled following friction test results performed at IFT-TU Wien as part of the CIRP working group activity. An inverted pin-on-disc-tests at elevated specimen temperatures up to 400°C reveal a cutting speed dependence. A linear fit for the friction coefficient, represented by the following equation and applicable to a Hertzian pressure of about 2140 MPa, was found for the range of 50 m/min to 300 m/min: $\mu = -0.0012 \cdot v_c + 0.54$. Simulations are performed with elevated tool temperature (650°C, determined by measurement) to emulate steady cutting conditions.

4. Experimental setup, cutting tests and DIC analysis

A DMG-MORI CTX gamma was used for the orthogonal cutting experiments. Fig. 4 shows the test setup. Disc-shaped specimens

[1] Certain commercial equipment, instruments, or software products are identified in this paper to adequately specify procedures and methods. Such identification is not intended to imply recommendation or endorsement by NIST.

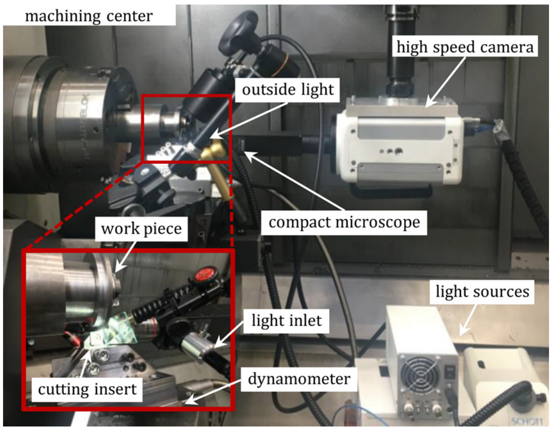

Fig. 4. Experimental test setup for orthogonal cutting.

with a width of 4 mm were cut of a bar of annealed AISI 1045 with a diameter of 80 mm and finally prepared by grinding, polishing and etching. The specimens were placed on a mounting adaptor, which was fixed in a three-jaw chuck. For the force measurement, the tool holder was mounted on a dynamometer (Kistler Typ 9129AA) and thus the cutting force and feed force were recorded. In the cutting tests, HC cutting inserts SCMW 120408 (corner radius $r_\varepsilon = 0.8$ mm), grade P25 coated with TiAlN, were used. The cutting inserts have a rake angle of $\gamma = 0°$ and a cutting edge radius $r_\beta = 30$ μm. The cutting speed was varied from 50 m/min to 300 m/min in steps of 50 m/min. Within this investigation, a feed rate of f = 0.3 mm was selected.

Each cutting test was repeated three times and the tool inserts were changed during the experiments to limit effects resulting from tool wear. The temperature on the backside of the chips was measured with a two-color pyrometer via a fiber optic cable. The cutting inserts were modified with a borehole for the fiber optic, 1.6 mm away from the cutting edge. To avoid the violation of the gray body assumption, the pyrometer was validated on machined chips heated in a furnace.

For the experimental investigations of the shear zone, 2D DIC measurements were performed using a high-speed camera (Photron S16) with a field of view of 1 mm x 1 mm. Images were taken at 150.000 fps with a resolution of 256 pixels x 240 pixels. Due to the 2D analysis, chip displacements out of plane were ignored. DIC patterning was accomplished by etching the specimen surface. The cutting inserts were ground plane on the side oriented towards the camera to improve the focus. The DIC analysis was performed using commercial DIC software (GOM Aramis). By following 21 pixel x 21 pixel subsets of the images, it was possible to determine displacements, velocities, strains and strain rates. The reference image is located in the middle of a sequence of 30 images. However, the average chip speed and chip compression ratio λ as well as the shear angle Φ were evaluated for different cutting speeds. By calculating the differences in the von Mises strains from one image to the next, strain rates were evaluated.

5. Comparison of simulation and experiments

In Fig. 5, the strain rate history of single material points through the cutting zone is tracked in the time domain. These results were achieved by DIC measurements and compared with 2D JC and m-PTW-0/-1 models. The point trajectories and the element sizes in the simulations are indicated in the upper right images, the lower right image shows the point path and the subset size in the DIC. Because the m-PTW-0/-1 solutions calculate a thinner chip compared to the JC model, the JC model trajectory deviates from the other trajectories. Both m-PTW models track the DIC result closely during the initial rise in strain rate but reach significantly higher peaks compared to the DIC result. This effect derives from the lower resolution of the DIC measurement compared to the simulation which smoothes results in the primary shear zone (see subset and element size in Fig. 5). In DIC measurements, the correlation typically uses only affine transformations of image subsets, and each measurement represents an average of neighboring subsets. Both effects are relevant due to the relatively low

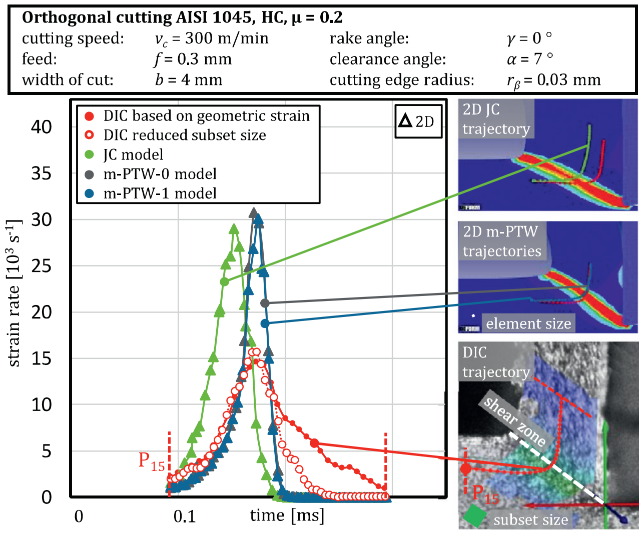

Fig. 5. Strain rate histories of individual material points on their way through the primary shear zone.

resolution of the high-speed images and the small size of the shear zone, causing the slow degradation of the strain rate. By taking the DIC data and calculating a reduced subset size (3 neighboring subsets instead of 6) the result shows the behavior of the narrow-resolution FEA. Additional errors occur at the cutting edge radius where the material separation causes an artificially large estimate of strain rate.

Fig. 6compares the 3D-simulated chip thickness against measurements taken at the center of the chips. The real chips were found to be thinner at the outer areas than in the center, indicating that the cutting experiment does not satisfy plane strain conditions. As a result, the focus will be on 3D rather than on 2D (plane strain) simulation results. The m-PTW models show good correlation at higher cutting speeds but poor correlation at the lowest speed. The JC model predicts thicker chips compared to the m-PTW models and the experiments with a consistent deviation compared to the experiments.

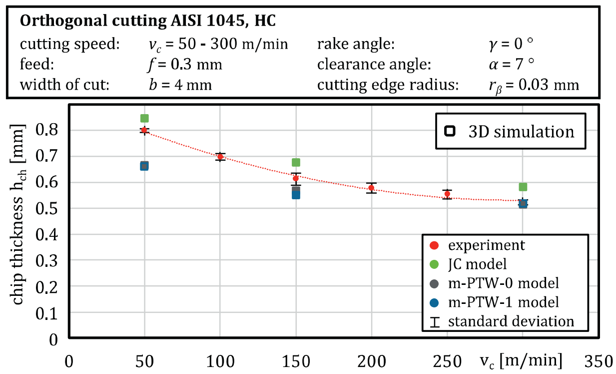

Fig. 6. Chip thickness of orthogonal cutting test and simulation results.

Fig. 7 plots cutting and feed force measurements compared with the 2D and 3D simulations using all models. The orthogonal cutting tests have a 4 mm width-of-cut. Standardized force values are calculated for a reference width of cut of 1 mm to compare 2D and 3D simulations and measurements. It is known from [11] that 2D models underestimate cutting forces by about 10% compared to 3D. All simulation results show decreasing cutting forces at increased cutting speeds in accord with experiment. The 3D JC model overestimates the cutting forces by more than 100 N, whereas the m-PTW-0 and the m-PTW-1 models predict the cutting forces to 50 N or better but under-estimate the feed forces by a larger amount compared with the JC model.

Fig. 8 depicts the measured (mean value from 3 repetitions) and simulated temperature evolution along the chip bottom in the time domain. The material passing through the shear zone exhibits a rapid

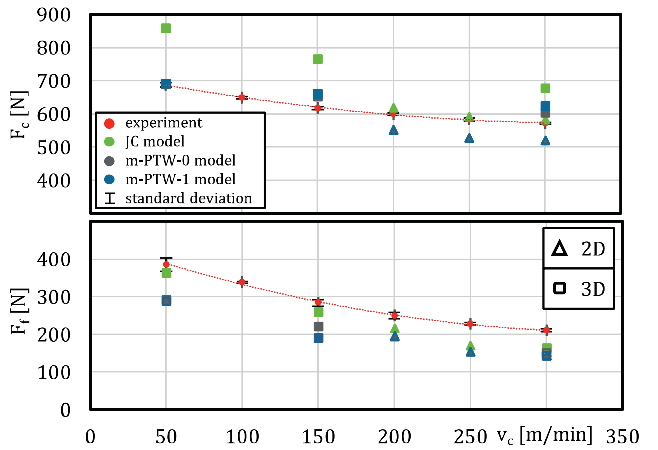

Fig. 7. Experimental and simulation results of standardized cutting forces F_c and feed forces F_f.

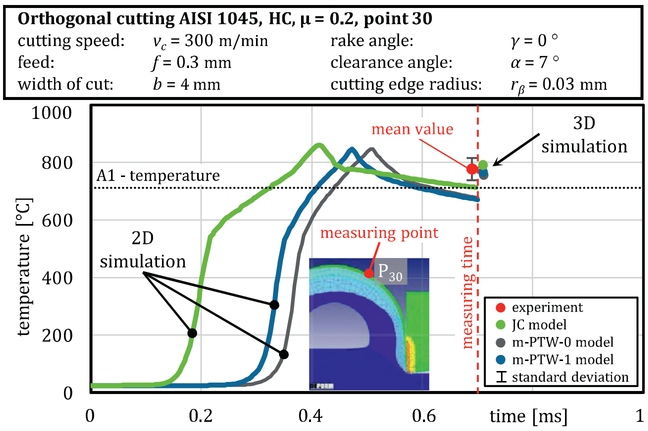

Fig. 8. Temperature results by measurements and simulation results.

temperature increase, exceeding the A1 temperature values around the secondary shear zone.

For v_c = 300 m/min, the temperature measurements and the simulation results show good correspondence. Temperatures from the 3D simulation results have been averaged over the width of cut, and the standard deviation for all simulated conditions is within ± 25°C.

Differences in modelled chip thicknesses and cutting forces between the JC and m-PTW models are associated with differences in the strain hardening behavior, shown in Fig. 9. Beyond 0.5 plastic strain, the m-PTW-0 model shows more rapid strain softening than the JC model owing to the different hardening models used (Voce versus power law). The m-PTW models are calibrated with experiments only to 0.6 strain, so the computational results are extrapolations. However, the Voce hardening achieves better agreement with

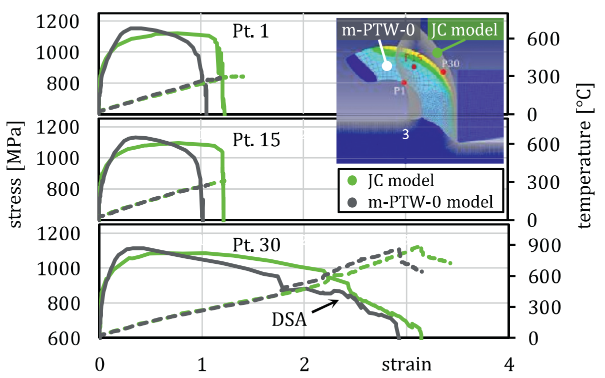

Fig. 9. Comparison of calculated stress (solid) and temperature (dashed) for JC (green) and m-PTW-0 (gray) 2D models at three positions. (For interpretation of the references to colour in this figure legend, the reader is referred to the web version of this article.)

cutting forces and chip thicknesses compared with the power law hardening at high cutting speeds in the more-realistic 3D simulation results. Higher workpiece strain hardening levels are known to result in larger chip thickness ratios, lower shear plane angles and higher cutting forces for identical friction conditions (cf. [12]). Finally, Fig. 9 demonstrates that DSA effects, which are captured in the m-PTW models, appear only in the chip root region and secondary shear zone where the combination of strain rate and temperature are in the necessary ranges. DSA effects do not appear in the primary shear zone for the present range of cutting conditions and are not captured by the JC model at all.

Finally, very little difference was noted between the m-PTW-0 and m-PTW-1 results, indicating little effect of heating time despite having calculated temperatures above A1 in the secondary shear zone. This outcome may be linked to work hardening retention through the phase transition, which is unavoidable in the current FEA calculation but may be unphysical. This point will be explored in future work. Also, because microstructural evidence of transformation is lacking, it is unclear whether transformation occurs under the tested conditions. However, fairly good agreement is nevertheless achieved with the m-PTW models and experiments at high cutting velocity despite the possibly unphysical transformation behavior.

6. Conclusion and outlook

The use of material models that consider effects of high heating rate and complex strain hardening show generally good agreement with orthogonal cutting experiments at high cutting speeds. The prediction of chip thickness, forces and temperatures matches well without any model adaptions made specifically to improve agreement. DIC shows promise in measuring the velocities and strain rates in the machining tests with relatively low noise levels and good agreement with simulations but higher image resolution is desirable. Increased adiabatic strain softening in with Voce hardening in the new model seems to improve chip morphology and cutting force predictions at high cutting speeds compared to power law hardening formulation in the JC model.

Declaration of Competing Interest

The authors declare that they have no known competing financial interests or personal relationships that could have appeared to influence the work reported in this paper.

References

[1] Robinson JM, Shaw MP (1994) Microstructural and mechanical influences on dynamic strain aging phenomena. *Int. Mater. Rev.* 39/3:113–122.
[2] Arrazola PJ, Özel T, Umbrello D, Davies M, Jawahir IS (2013) Recent advances in modelling of metal machining processes. *CIRP Ann. - Manuf. Technol.* 62/2. 695–71.
[3] Childs THC, Otieno AW (2012) Simulations and experiments on machining carbon and low alloy steels at rake face temperatures up to 1200°C. *Mach. Sci. Technol.* 16:96–110.
[4] Childs THC (2019) Revisiting flow stress modelling for simulating chip formation of carbon and low alloy steels. *Proc. CIRP* 82:26–31.
[5] Mates SP, Vax E, Rhorer RR, Stoudt MR (2020) Dynamic flow stress behavior of hypoeutectoid ferrite-pearlite steels under rapid heating. *J. Dynamic Behav. Mater.* 6/2:246–265.
[6] Speich GR, Demarest VA, Miller RL (1981) Formation of austenite during intercritical annealing of dual-phase steels. *Metall. Trans. A* 12A:1419–1428.
[7] Preston DL, Tonks DL, Wallace DC (2003) Model of plastic deformation for extreme loading conditions. *J. Appl. Phys.* 93/1:211–220.
[8] Vural M, Rittel D, Ravichandran G (2003) Large strain mechanical behavior of 1018 cold-rolled steel over a wide range of strain rates. *Metall. Trans. A* 34A:2873–2885.
[9] Mates SP, Li S-Y A Dynamic Plasticity Model for Rapidly-Heated 1045 Steel up to 1000°C, submitted to Mechanics of Materials
[10] Jaspers SPFC, Dautzenberg JH (2002) Material behaviour in conditions similar to metal cutting: flow stress in the primary shear zone. *J. Mater. Process. Technol.* 122/2-3:322–330.
[11] Meyer LW, Halle T, Herzig N (2005) Determination of special material behaviour and development of constitutive equations for numerical simulations of high speed cutting processes. *CIRP Proceedings - 8th International Workshop on Modeling of Machining Operations*, 131–138.
[12] Childs THC, Maekawa K, Obikawa T, Yamane Y (2000) *Metal Machining Theory and Applications*, John Wiley & Sons. New York ISBN 0 470 39245 2.